Appl. Phys. B 34, 107–122 (1984)

Applied Physics B Photophysics and Laser Chemistry

Optical Four-Wave Mixing in Epitaxial Narrow-Gap Semiconductor Films

H. Pascher

Physikalisches Institut, Universität, D-8700 Würzburg, Fed. Rep. Germany

Received 17 January 1984/Accepted 12 March 1984

Abstract. A short review on the theoretical description of nonlinear optical phenomena which are caused by an electric polarization cubic in the electric field amplitudes is given. Then the microscopic theories for the calculation of the nonlinear susceptibility, especially in semiconductors, are briefly reported. After a short section on the bandstructure of IV–VI compounds in a magnetic field, the lineshapes of the coherent anti-Stokes radiation as a function of the magnetic field are discussed in detail.
In the experimental part measurements of coherent anti-Stokes Raman scattering (CARS) in PbTe and PbSe epitaxial films are reported. We observed pure as well as combined spin flip transitions. These data and the results of additionally observed interbandtransitions were used in least squares fits and consistent sets of bandparameters of PbTe and PbSe were obtained.

PACS: 42.65, 71.20

The first theoretical work on nonlinear optical phenomena was done by Göppert-Mayer already in 1931 [1]. But the processes described there could not be found experimentally, since lasers had been discovered. Soon after the first observation of second-harmonic generation [2] in 1961, Bloembergen and co-workers developed the theory of the propagation of electromagnetic waves in nonlinear media. This work is summarized in *Nonlinear Optics* [3]. A quantum-mechanical treatment of the nonlinear susceptibilities has been given in several publications, e.g. [4–6].
There are two important applications of nonlinear optical processes in spectroscopic applications. First these processes may yield coherent radiation with frequencies where no laser lines are available. This is of great importance in the infrared and ultra-violet, where no tunable lasers work. Second, the polarization selection rules for nonlinear interactions of light with matter often are different from the linear ones and other transitions are observable in the nonlinear experiments.
One kind of such investigations are the four-wave-mixing experiments where two laser beams with frequencies ω_1 and $\omega_2 = \omega_1 - \Delta\omega$ are superposed in a sample and additionally yield radiation with frequencies $\omega_1 + \Delta\omega$ (coherent anti-Stokes Raman scattering: CARS) and $\omega_2 - \Delta\omega$ (coherent second Stokes Raman scattering) [7].
CARS has developed to a very useful technique to obtain the Raman spectra of different materials. Though Patel et al. [8] observed the effect for the first time in InSb in 1966, up to now little work was done with narrow-gap semiconductors and in the infrared. There are reports on the spin- and cyclotron resonances of the four-photon mixing in InSb by Yablonovitch et al. [9], Wynne [10], Nguyen et al. [11], and Bresler et al. [12] and in $Hg_{1-x}Cd_xTe$ by Bridges et al. [13] but they did not use the results for the determination of band parameters of the semiconductors. This was done by Pascher in InAs [14]. Aggarwall reported on four-wave mixing spectroscopy of shallow donors in Ge [15]. For a general review, see [16].
In this paper the applications of CARS in infrared spectroscopy of narrow-gap semiconductors will be discussed. As examples we used epitaxial films of PbTe and PbSe, respectively. Though there is a lot of experimental and theoretical work done on these

compounds (see, e.g., the review of Bauer [17] and the literature cited there) still exist discrepancies on the band parameters of these semiconductors. This may be due to the fact that all authors have observed either interband- or intraband transitions and none of them has used both kinds of information to fit their parameters. The other reason may be that the absorption spectra in the far infrared are strongly influenced by plasmon and phonon effects and therefore the effective masses have to be calculated by a complicated fitting procedure that increases the experimental errors.

CARS experiments can be done in a spectral range, where no plasmons or phonons are present. Due to the high powers available, CO_2 lasers are very well suited. Pure and combined spin-flip resonances in an external magnetic field yield narrow lines from which the intraband-transition energies can be deduced very precisely.

But there are also some difficulties in the interpretation of the spectra arising from complicated lineshapes. Therefore in this paper we present a detailed discussion of the lineshapes of different kinds of resonances as they arise from the real and imaginary part of the nonlinear susceptibility and from changes in the occupation of states involved in the scattering process, caused by the nonlinear interaction.

1. Theory

In this section we give a short summary on Bloembergen's classical theory of the coupling of four electromagnetic waves in a medium by a third-order nonlinear susceptibility [3], and on the calculation of this susceptibility of semiconductors; and we show different kinds of resonances of the susceptibility. Further the calculation of the Landau levels of IV–VI compounds after Mitchell and Wallis [18] is reported briefly. The section is closed by the discussion of the lineshapes of different kinds of magnetooptical intrabandtransitions, as calculated for the CARS intensity.

1.1. Classical Theory

The nonlinear processes, caused by electromagnetic waves of high intensity propagating through a medium can be described by a power series of the polarization **P**:

$$P_i = \varepsilon_0(\chi_{ij}^{(1)}E_j + \chi_{ijk}^{(2)}E_jE_k + \chi_{ijkl}^{(3)}E_jE_kE_l + \ldots). \tag{1}$$

In media with inversion symmetry the lowest-order nonlinear terms in these expansions are the cubic ones.

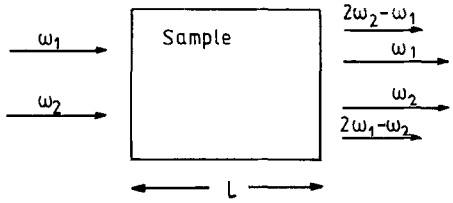

Fig. 1. Schematic diagram of the assumed experimental situation

In the following we are concerned with the polarization which is cubic in the fields. We call it P^{NL}

$$P_i^{NL} = \varepsilon_0\chi_{ijkl}E_jE_kE_l. \tag{2}$$

The electric field of an electromagnetic wave with frequency ω is

$$\mathbf{E}(\mathbf{r},\omega,t) = \{\mathbf{E}(\mathbf{r},\omega)\exp[\mathrm{i}(\mathbf{k}\cdot\mathbf{r}-\omega t)] + \text{c.c.}\}/2. \tag{3}$$

From Maxwell's relations the well known wave equation is deduced

$$\Delta\mathbf{E} = \mu_0\sigma\frac{\partial\mathbf{E}}{\partial t} + \mu_0\varepsilon_0\varepsilon_r\frac{\partial^2\mathbf{E}}{\partial t^2} + \mu_0\frac{\partial^2\mathbf{P}^{NL}}{\partial t^2}. \tag{4}$$

Further calculations are done with the following assumptions and approximations, respectively:

a) The waves are propagating in x-direction.

b) Absorption is neglected.

c) Second derivatives of the electric fields are neglected:

$$|\partial^2E(x,\omega)/\partial x^2| \ll |k\,\partial E(x,\omega)/\partial x|.$$

d) The amplitudes of the fields radiated onto the sample do not change with respect to space. This means that the power transfered to the scattered beams is neglected.

With these approximations the wave-equation becomes (noted for the i^{th} component)

$$\mathrm{i}k_x\frac{\partial E_i(x,\omega)}{\partial x} = \mu_0\frac{\partial^2P_i^{NL}}{\partial t^2}\mathrm{e}^{-\mathrm{i}(k_xx-\omega t)}. \tag{5}$$

Further, we shall consider the experimental situation, as schematically drawn in Fig. 1. Two laser beams with frequencies ω_1 and ω_2, $\omega_1 > \omega_2$ are collinearly focussed onto a sample with the length L. The radiation leaving the sample is fed into a grating monochromator and the intensity at $\omega_3 = 2\omega_1 - \omega_2$ is measured. According to incoherent Raman scattering we also call the frequencies $\omega_L := \omega_1$, $\omega_S := \omega_2$, and $\omega_{AS} := \omega_3$ where the indices stand for (pump-) laser, Stokes, and anti-Stokes frequencies. Two effects will be discussed in detail:

Coherent Anti-Stokes Raman Scattering

The intensity of the wave with frequency ω_{AS} at the end of the sample can be calculated by solving the wave

equation (5). The result is

$$I_{AS}=L^2\frac{9}{16}\frac{\omega_{AS}^2}{c^4 n_{AS}n_L^2 n_S\varepsilon_0^2}|\chi|^2 I_L^2 I_S \cdot\left(\frac{\sin(\Delta\mathbf{k}\cdot\mathbf{x}_0 L/2)}{\Delta\mathbf{k}\cdot\mathbf{x}_0 L/2}\right)^2 \quad (6)$$

($\Delta\mathbf{k}=2\mathbf{k}_L-\mathbf{k}_S-\mathbf{k}_{AS}$; $\mathbf{x}_0$ vector of unit length in x-direction).

The CARS intensity is proportional to the square of the sample length. Therefore it is expected to be very difficult to observe the effect in thin epitaxial layers of a "length" of a few μm.

If the laser beams propagate collinearly and the medium has normal dispersion then the phasefactor $\sin(\Delta\mathbf{k}\cdot\mathbf{x}_0 L/2)/\Delta\mathbf{k}\cdot\mathbf{x}_0 L/2$ is less than unity. The intensity has a maximum if the length of the sample is equal to the coherence length $L_c=\pi/\Delta k$. Since the main concern of the present work is the application of CARS on epitaxial films with $L\ll L_c$ in the following the phase factor is approximately one.

Raman Gain

Raman amplification in semiconductors was discussed in [19–21]. We recognize the field that oscillates with the frequency ω_S. The solution of (5) is

$$I_S(x)=I_S(0)\exp[(g_S I_L-\alpha_S)x] \quad (7)$$

with the Raman gain g_S being proportional to the imaginary part of the third-order nonlinear susceptibility. One important feature of (7) is that there is no phase factor. The growth of Stokes intensity per unit length is proportional to the Raman gain and in turn to the imaginary part χ'' of the susceptibility. It is also proportional to the power of the pump laser. If the resonance is due to an electronic transition in a semiconductor each scattered photon leaves an electron in the upper level. With high laser powers this can produce a change in the occupation of the levels which is no longer neglectable. The change of the number of electrons in the lower level is

$$\Delta N_u\propto|\chi''|. \quad (8)$$

1.2. Nonlinear Susceptibility in Semiconductors

Nonlinearity Due to the Nonparabolicity of the Conduction Band

As noted in the introduction, Patel et al. [8] observed optical mixing in the narrow-gap semiconductors InSb and InAs for the first time. Wolff and Pearson [22] developed a theory based on a classical Drude model [23] and on the non-parabolicity of the bands which described the experimental findings of Patel et al. The susceptibility calculated by Wolff is real and has no

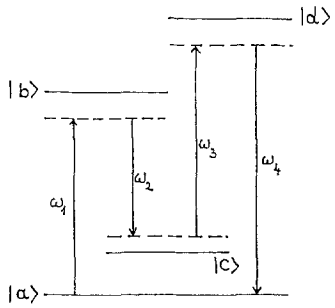

Fig. 2. Energy level diagram. General case with incident waves with 3 different frequencies

resonances caused by transitions in the semiconductor, i.e.

$$\chi^{(3)\,NR}=\frac{N_0 e^4}{4(m^*)^2 E_g\omega_L^2\omega_S\omega_{AS}\varepsilon_0}\cdot\frac{1+8E_F/5E_g}{(1+4E_F/E_g)^{5/2}}. \quad (9)$$

As can be seen from (9) the non-resonant mixing must be strong in narrow-gap semiconductors since the gap energy and the effective mass are small quantities in the denominator. As long as the carrier density is not too large ($E_F\ll E_g$) the non-resonantly scattered intensity is proportional to the square of the carrier concentration.

Quantummechanical Calculation of the Third-Order Nonlinear Susceptibility

There is a large number of papers which present theoretical treatments of nonlinear optical processes (see the review of Eesley [24] and literature cited there). An expression for $\chi^{(3)}$ is given in [Ref. 24, Table A2]. This calculation is based on the optical transitions as schematically drawn in Fig. 2. In our further discussion the levels are electronic states in a semiconductor. N_a is the density of electrons in the lower level $|a\rangle$. If there are other states, e.g. $|c\rangle$ occupied, then there are other 24 terms to be added to the terms denoted in [24].

i) One-Photon Resonance of the Susceptibility. If in the atomic system there is a level $|b\rangle$ with $\omega_{ba}=\omega_1$ and the transition from the ground level $|a\rangle$ to $|b\rangle$ is allowed and if the radiation with frequency ω_1 has the proper polarization, then six of the 24 terms of the susceptibility are resonantly enhanced. This is demonstrated by the experimental result shown in Fig. 3. The picture shows the increase of the third-order nonlinear susceptibility of InSb when $\hbar\omega_1$ approaches the energy gap of 1896 cm^{-1}.

ii) Two-Photon Resonance of the Susceptibility. If $\omega_{ca}=\omega_1+\omega_3$ another 4 terms are enhanced. Figure 4 shows an experimental example. In this figure magneto-optical interband transitions in InSb are involved. The resonances of the four-wave mixing signal occur at those magnetic fields, at which two-

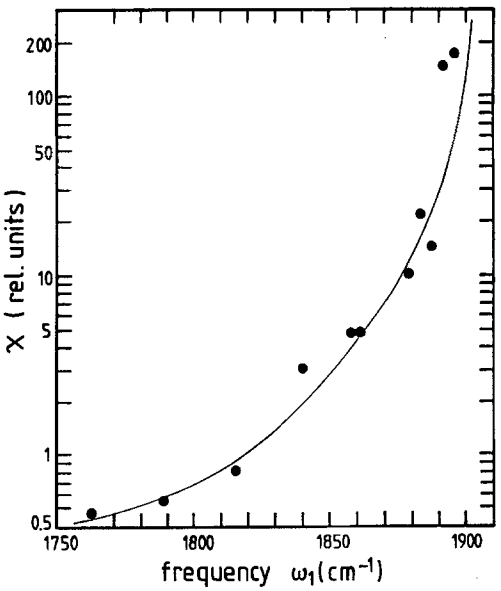

Fig. 3. Measured resonance of the third-order nonlinear susceptibility caused by one-photon transitions in InSb

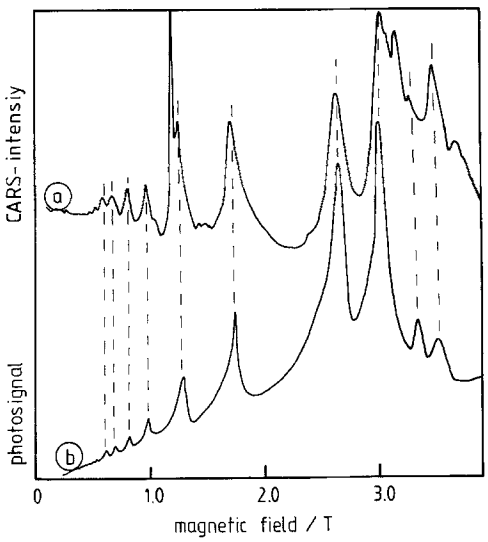

Fig. 4a and b. Measured two-photon resonances of the third-order nonlinear susceptibility of InSb in a magnetic field. (a) CARS intensity. (b) Two-photon absorption indicated by photoconductivity

photon allowed interband transitions reach an energy of $2\hbar\omega_1$. This is demonstrated by comparing the resonant magnetic fields of Fig. 4a with the resonances in a two-photon absorption measurement by photoconductivity, carried out by Richter with the same laser frequency [25].

iii) Raman-Resonances of the Susceptibility-CARS. The resonances of the terms 1, 2, 7, and 8 [Ref. 24, Table A2] are the main concern of the present work and shall be discussed in more detail (Fig. 5). If among

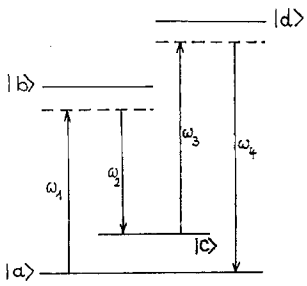

Fig. 5. Energy level diagram for Raman resonances

the intermediate states $|c\rangle$ there is one with $\omega_{ca}=\omega_1-\omega_2$ and the product of matrixelements [Ref. 24, Table A2] is not equal zero, then this term will dominate the others and we can omit the summation upon c. The imaginary parts of the other factors in the denominators can be neglected if no other resonances occur. Thus we may simplify the formula given in [24]:

$$\chi^{(3)}_{ijkl}(-\omega_4,\omega_1,-\omega_2,\omega_3) = \frac{-N_a}{6\hbar^3\varepsilon_0}\left[\frac{1}{\omega_{ca}-\omega_1+\omega_2-i\Gamma_{ca}}\sum_{b,d}\left(\frac{\mu_{jkli}}{(\omega_{ba}-\omega_1)(\omega_{da}-\omega_4)} + \frac{\mu_{jkil}}{(\omega_{ba}-\omega_1)(\omega_{da}+\omega_3)} + \frac{\mu_{kjli}}{(\omega_{ba}+\omega_2)(\omega_{da}-\omega_4)} + \frac{\mu_{kjil}}{(\omega_{ba}+\omega_2)(\omega_{da}+\omega_3)}\right)\right] + \chi^{NR}. \quad (10)$$

The abbreviation μ_{ijkl} stands for a product of four dipol matrixelements $\mu_{ab}\mu_{bc}\mu_{cd}\mu_{da}$ with the field polarizations i, j, k, l. $\omega_{\alpha\beta}$ is equal to $(E_\alpha-E_\beta)/\hbar$. $\Gamma_{\alpha\beta}$ is the homogeneous linewidth of the transition $\alpha\rightarrow\beta$.

χ^{NR} is the summ over the other 20 terms and is real. The contribution in χ^{NR} dominating in narrow-gap semiconductors has been calculated above.

Up to now it has been assumed that only the initial matter state $|a\rangle$ is occupied. If other states, e.g. $|c\rangle$, are significantly poulated, additional 24 terms, summed over a, b, and d have to be added. These terms can be deduced from the listed ones if one exchanges ω_1 and ω_2 and the states $|a\rangle$ and $|c\rangle$, respectively. Considering $\omega_{ca}=-\omega_{ac}$ it is seen that the expression in brackets, (10), changes its sign.

The terms noted in (10) may be identified with Stokes scattering of the radiation with frequency ω_1, the additional terms arising from a occupation of level $|c\rangle$ with anti-Stokes scattering of the radiation with ω_2. We now introduce the abbreviation M for the expression $\Sigma(\ldots)$ in (10) and find as result for the susceptibility if states $|a\rangle$ and $|c\rangle$ are populated:

$$\chi^{(3)}_{ijkl}(-\omega_4,\omega_1,-\omega_2,\omega_3) = \frac{-(N_a-N_c)}{6\hbar^3\varepsilon_0}\frac{1}{\omega_{ca}-\omega_1+\omega_2-i\Gamma_{ca}}M+\chi^{NR}. \quad (11)$$

Table 1. Band parameters in Mitchell and Wallis notation

Two-band parameters		Farband parameters	
E_g	energy gap	m_t^+/m_0	contribution of the four remote bands to the transverse mass of the valenceband
$2P_\perp^2/m_0$	interbandmatrixelement	m_t^-/m_0	contribution of the four remote bands to the transverse mass of the conductionband
a_{cv}	$P_\perp/P_\parallel$ ($\perp$ and $\parallel$ are related to $\langle 111\rangle$)	$a^+=(m_l^+/m_t^+)^{1/2}$	
		$a^-=(m_l^-/m_t^-)^{1/2}$	
		g_t^+, g_l^+	contribution of the four remote bands to the transverse and longitudinal g-factor, respectively, of the valenceband
		g_t^-, g_l^-	contribution of the four remote bands to the transverse and longitudinal g-factor, respectively, of the conductionband

M does not significantly depend on the frequency. Separating real and imaginary part of the susceptibility the final result is

$$\chi=\chi^{\mathrm{NR}}+\chi'+\mathrm{i}\chi'', \tag{12}$$

where

$$\chi'=\frac{-(N_a-N_c)}{6\hbar^3\varepsilon_0}M\frac{\omega_{ca}-\omega_1+\omega_2}{(\omega_{ca}-\omega_1+\omega_2)^2+\Gamma_{ca}^2} \tag{13}$$

and

$$\chi''=\frac{-(N_a-N_c)}{6\hbar^3\varepsilon_0}M\frac{\Gamma_{ca}}{(\omega_{ca}-\omega_1+\omega_2)^2+\Gamma_{ca}^2}. \tag{14}$$

The CARS intensity is proportional to the square of the susceptibility

$$|\chi|^2=|\chi^{\mathrm{NR}}|^2+|\chi'|^2+|\chi''|^2+2\chi^{\mathrm{NR}}\chi'. \tag{15}$$

In this section we discussed the most general case with waves with three different frequencies radiated onto the sample. The case as assumed in Fig. 1 results if one puts in all equations $\omega_3=\omega_1=\omega_L$ and $\omega_4=\omega_{\mathrm{AS}}$.
The lineshape of the CARS intensity in the vicinity of a Raman resonance is, in general, complicated, since there is an interference between resonant and non-resonant contributions. With Raman resonances of the electronic system of a semiconductor besides this interference Fermi statistics and changes in the occupation of the states by nonlinear effects like Raman gain have to be taken into account.

1.3. Band Structure of IV–VI Compounds in a Magnetic Field

A complete review on the calculations of the band structure of IV–VI compounds and the experimental results obtained up to now has been given by Bauer [17]. In this section the facts used in the following are placed together.
The compounds have a direct gap at the L-point of the Brillouin zone. To calculate the Landau levels one can use the $\mathbf{k}\cdot\mathbf{p}$ treatment by Mitchell and Wallis [18]. In this scheme the energies of the levels are obtained by diagonalization of a 4×4 matrix which e.g. is given in [17].
In the model there are included 11 parameters which are listed in Table 1. Effective g-values and masses are obtained from the band parameters by (16)–(21), i.e.,

$$g^*(\theta)=(g_l^2\cos^2\theta+g_t^2\sin^2\theta)^{1/2}, \tag{16}$$

$$\omega_c(\theta)=eB\left(\frac{\sin^2\theta}{m_lm_t}+\frac{\cos^2\theta}{m_t^2}\right)^{1/2}, \tag{17}$$

$$\frac{1}{m_t^{cb}}=\left(\frac{2P_\perp^2}{m_0}\right)\frac{1}{E_g}+\left(\frac{m_t^-}{m_0}\right)^{-1}, \tag{18}$$

$$\frac{l}{m_l^{cb}}=\left(\frac{2P_\perp^2}{m_0a_{cv}^2}\right)\frac{1}{E_g}+\left(\frac{m_t^-(a^-)^2}{m_0}\right)^{-1}, \tag{19}$$

m_l^{cb}, m_t^{cb}: conductionband masses; analogous formula valid for valenceband,

$$g_l^{cb}=2\left(\frac{2P_\perp^2}{m_0}\right)\frac{1}{E_g}+g_l^-, \tag{20}$$

$$g_t^{cb}=2\left(\frac{2P_\perp^2}{m_0a_{cv}}\right)\frac{1}{E_g}+g_t^-, \tag{21}$$

g_l^{cb}, g_t^{cb}: conductionband g-factors; analogous formula for valenceband.
The bands have a many-valley structure consisting of four ellipsoids oriented along the $\langle 111\rangle$ axis. Epitaxial films on BaF_2 substrates are grown with the $\langle 111\rangle$ direction perpendicular to the sample surface. In optical experiments in Faraday configuration **B** is parallel to $\langle 111\rangle$. In Voigt configuration there are two

Table 2. Angles θ between ellipsoid axis and magnetic field

Configuration	Angle θ	Number of ellipsoids
$\mathbf{B}\parallel\langle 111\rangle$	0°	1
(Faraday)	70.53°	3
$\mathbf{B}\parallel\langle 110\rangle$	35.26°	2
(Voigt)	90°	2
$\mathbf{B}\parallel\langle 211\rangle$	19.47°	1
(Voigt)	61.81°	2
	90°	1

distinguished orientations of the magnetic field, namely $\mathbf{B}\parallel\langle 110\rangle$ and $\mathbf{B}\parallel\langle 211\rangle$. With these orientations we find the angles θ between the axis of the ellipsoids and the magnetic field which are noted in Table 2.

Polarization selection rules for magnetooptical inter- and intrabandtransitions are calculated by Zawadzki [26, 17]. Table 3 gives a survey on the allowed electric dipole transitions.

In Fig. 6 a schematic drawing of the Landau levels as a function of the magnetic field is given. The arrows indicate transitions allowed in Voigt configuration. The scheme on the right hand side gives the ordering of intermediate states (compare Fig. 5) for calculating the contributions to $\chi^{(3)}$, arising from the spin-flip process in the valence band. From the interband-selection rules it is seen that the radiation with ω_L and ω_S has to be polarized perpendicular to one another. Then the spin flip transition is the strongest Raman-resonance of the semiconductor.

1.4. Lineshapes of Raman-Resonances of the CARS Intensity due to Magnetooptical Intrabandtransitions in Semiconductors

The considerations of this section are based on Eqs. (6, 13–15). The susceptibility $\chi^{(3)}$ has a nonresonant term χ^{NR} caused by the nonparabolicity of the bands. This term does not depend noticeably on an external magnetic field. Additionally, there are resonant contributions if $\omega_1-\omega_2$ is within the linewidth of a Raman transition of the scattering medium. In the examples to be discussed now this is the spin resonance: $\hbar(\omega_1-\omega_2)=g^*\mu_B B$. In the following calculations a g-value of 15, a frequency difference $\omega_1-\omega_2$ of 28 cm^{-1} and a linewidth of 2 cm^{-1} is assumed. These values result in a resonant magnetic field of 4 T and a linewidth of about 0.3 T.

With the calculation of the lineshape, that means the dependence of the CARS intensity on the magnetic field in the vicinity of the resonance in general the following parameters have to be taken into account:

i) The Carrier Density N and the Value of the Resonant Magnetic Field. These values determine the relative occupation of the two spin states. With high carrier density and low magnetic field the two levels are almost equally populated. For high magnetic fields larger than the quantum limit B_Q (depending on N) only the lower level is occupied. The non-resonant susceptibility is proportional to N, see (9).

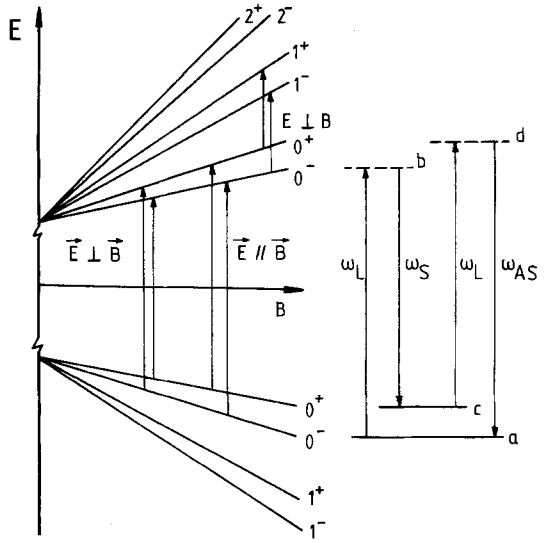

Fig. 6. Schematic drawing of Landau levels as a function of the magnetic field and corresponding energy level diagram for spin-flip transitions in the valence band

Table 3. Polarization selection rules [17]

Polarization	E_z		E_-		E_+	
Transition	Δn	Δs	Δn	Δs	Δn	Δs
1-photon			0	+1	0	−1
Interband	0	0	+2	−1	−2	+1
2-photon	+1	−1	+1	+1	−1	−1
Interband	−1	+1	+3	−1	−3	+1
1-photon	+1	−1	+1	0	−1	0
Intraband	−1	+1	0	+1	0	−1

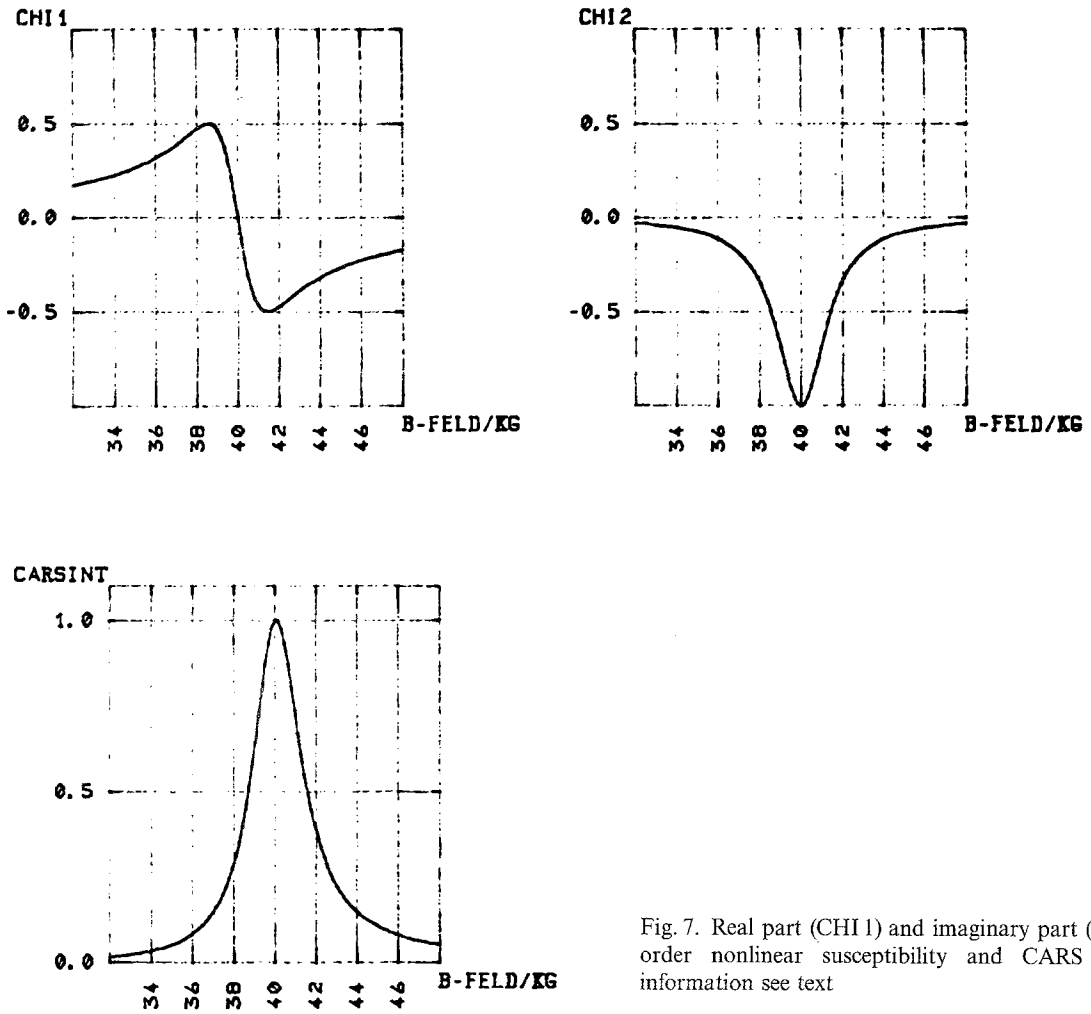

Fig. 7. Real part (CHI 1) and imaginary part (CHI 2) of the third-order nonlinear susceptibility and CARS intensity. Further information see text

ii) The Power of the Pump Lasers. The intensities I_L and I_S which are explicitely included in (6) do not affect the lineshape. This section is concerned with the influence of the laser power on the occupations $\dot{N}_a$ and N_c. Free carrier absorption with high pump intensities decreases the value $N_a - N_c$. Due to multy-photon interband absorption and proper relaxation mechanisms it can occur that in the upper spin level is a larger carrier density than in the lower.

iii) The Raman Gain. By Raman amplification the difference $|N_a - N_c|$ is decreased proportional to χ'', see (8). From (7) it has been deduced that the growth of the Stokes intensity and therefore the change of occupation caused by this effect is proportional to I_L whereas the CARS intensity is proportional to I_L^2. Therefore this effect will be important even with moderate laser powers.

Additionally, with the Raman gain no phase factor has to be taken into account. Therefore the effect will play an important role if there is a large dispersion as is the case if $\hbar\omega_1$ and $\hbar\omega_2$ are near by the gap energy of the semiconductor or if the frequency difference $\omega_1 - \omega_2$ is large.

The following figures show some typical lineshapes, as they are calculated with different conditions. Real and imaginary part of the susceptibility are normalized such that $\chi'' = -1$ if all carriers were in the lower spin level. The CARS intensity is calculated according to (6) with χ from (11) and normalized to unity without respect to the absolute value.

In Fig. 7 is assumed that all carriers are in the lower level, the resonant contributions are very strong compared to χ^{NR} and the carrier density is large enough that changes due to Raman gain can be neglected. This situation is realized in doped semiconductors, with high magnetic fields and not too large laser intensities. The result is a nearly symmetric line with a maximum at the resonant magnetic field B_R. (Definition of B_R: $\hbar(\omega_1 - \omega_2) = g^* \mu_B B_R$.)

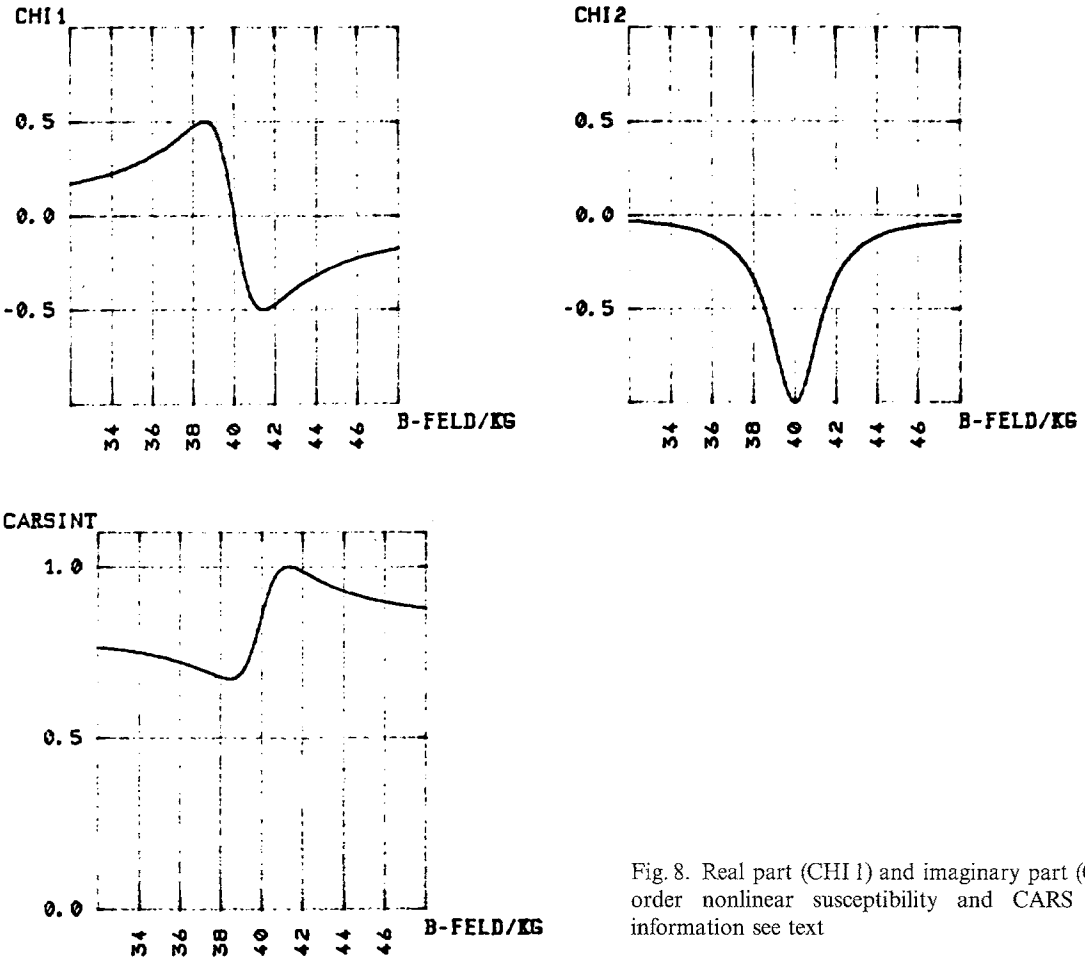

Fig. 8. Real part (CHI 1) and imaginary part (CHI 2) of the third-order nonlinear susceptibility and CARS intensity. Further information see text

In Fig. 8 the same assumptions are underlied as in Fig. 7 but the resonance is weak compared to the non-resonant contributions. This is the case if the transition $|a\rangle \rightarrow |c\rangle$ is not a strong Raman transition as, e.g., a cyclotron- or a combined spin- flip resonance. The lineshape demonstrated here also can be found if a few photoexited carriers in an unpopulated band have a resonance and many carriers in another band produce a strong non-resonant mixing. An example are photoexited carriers in the conduction band of a p-doped semiconductor.

Now the term $2\chi^{NR}\chi'$ dominates. The resonance is at the point of inflection of the steep increase of the curve.

Figures 9 and 7 differ by the assumption that the Raman gain shall cause a noticeable change of the occupation of the levels. This may occur if only a small number of electrons is in the lower level as it happens in a multy valley semiconductor in the valleys with small effective masses. This is also the case if due to additional one-photon resonances, the imaginary part of the susceptibility becomes very large, see (8). The doubling characteristic of the spin resonance observed by Bridges et al. [13] in $Hg_{1-x}Cd_xTe$ may be caused by this effect rather than by inhomogeneities in their samples. As will be shown in the experimental part we also observed such lineshapes in very homogeneous PbTe epitaxial films.

In the calculation od Fig. 10 the upper level $|c\rangle$ is assumed to have a higher occupation than $|a\rangle$. We already mentioned that this can be the case with very high laser powers. Additionally, Raman gain is recognized. Since the difference $N_c - N_a$ is taken to be very small the resonance can hardly be seen in χ' and χ''. The Term $2\chi^{NR}\chi'$ enables us to observe the resonance.

2. Experiments

2.1. Experimental Arrangement

A schematic diagram of the experimental setup is given in Fig. 11. Two single-frequency CO_2 lasers (frequencies ω_L and ω_S, respectively) were simultaneously Q-switched by mirrors mounted on the

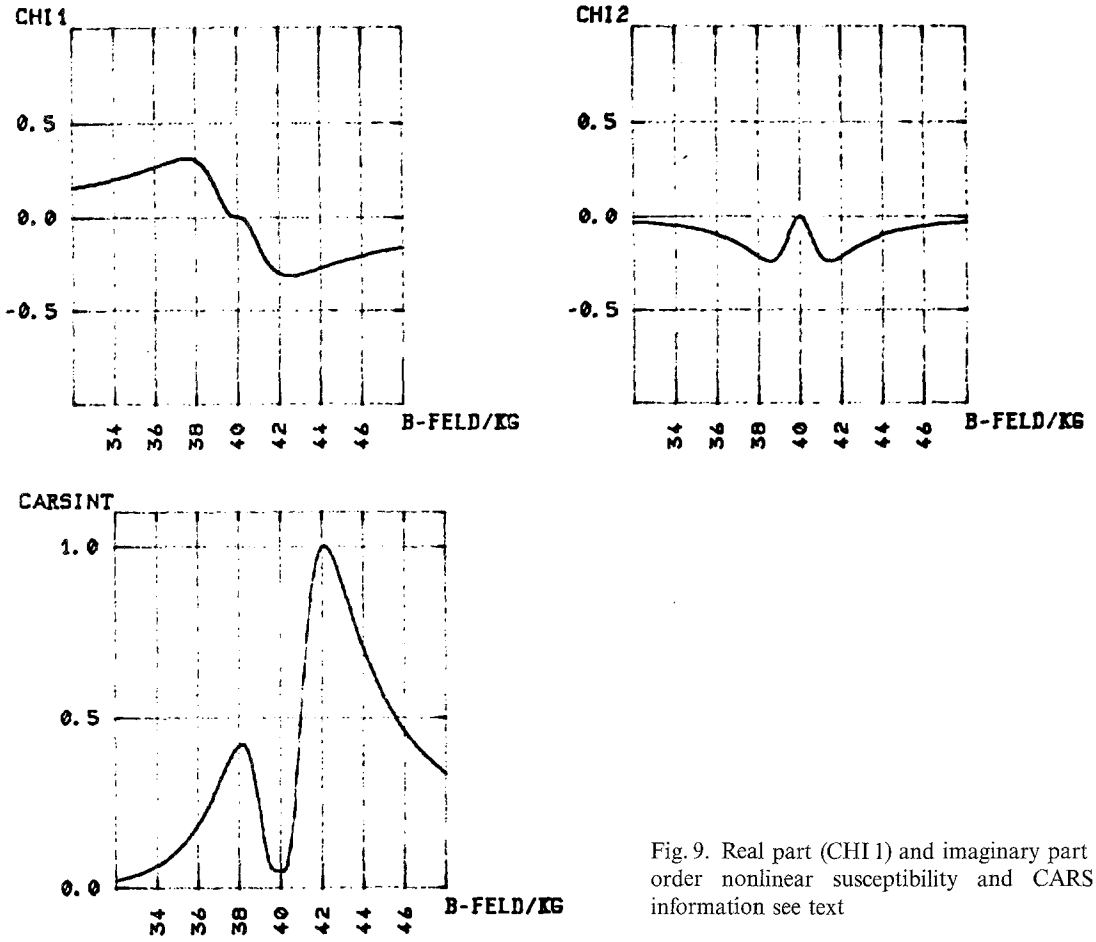

Fig. 9. Real part (CHI 1) and imaginary part (CHI 2) of the third-order nonlinear susceptibility and CARS intensity. Further information see text

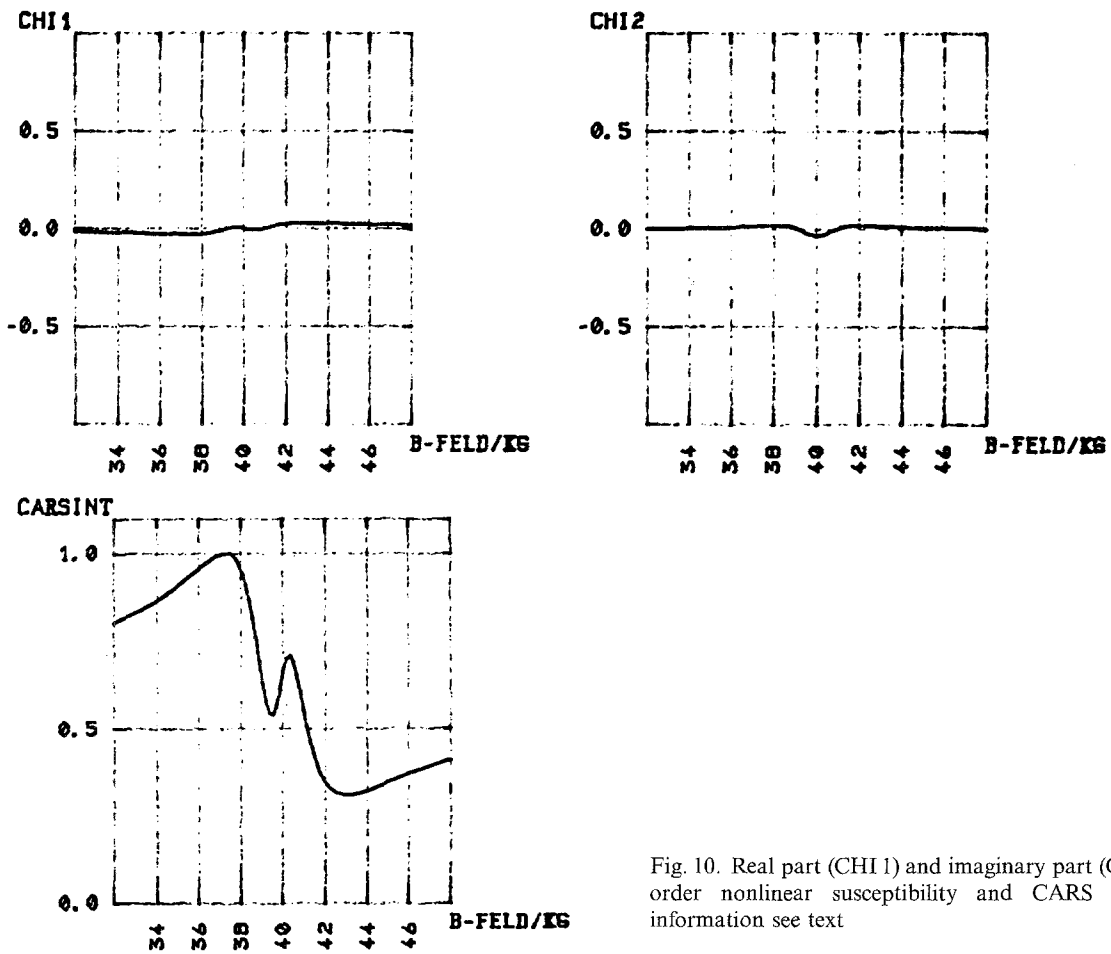

Fig. 10. Real part (CHI 1) and imaginary part (CHI 2) of the third-order nonlinear susceptibility and CARS intensity. Further information see text

opposite sides of a rotating shaft. The peak powers of the lasers were, depending on the line, between 0.5 and 3 kW. The lasers operated on the TEM_{00} mode. For the evaluation of the experiments exact frequencies were taken from [27].

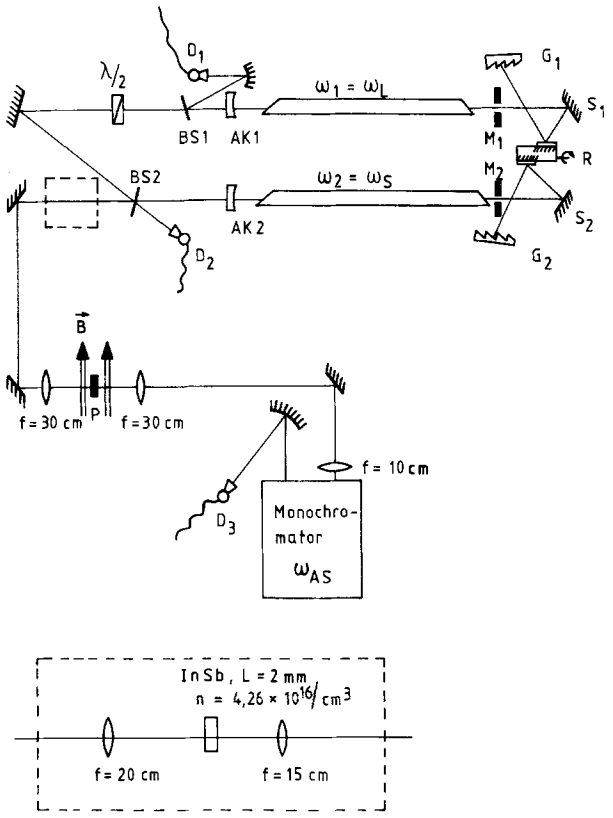

Fig. 11. Schematic diagram of the optical alignment (S_1, S_2: fixed mirrors; R: rotating mirror; G_1, G_2: gratings; M_1, M_2: diaphragm for single mode operation; AK_1, AK_2: output couplers; BS_1, BS_2: beam splitters; D_1, D_2, D_3: detectors; P: sample). For transmission measurements with radiation generated by four-wave mixing, the apparatus drawn within the dashed lines in the lower part is inserted at the place marked by dashed lines behind BS_2

In the CARS experiments the radiation of these lasers was collinearly focussed (focal length 30 cm) onto the sample (epitaxial layer on BaF_2, sample normal parallel ⟨111⟩). With the aid of half-wave plates the desired polarization of the lasers was achieved. The sample was mounted in Voigt configuration ($\mathbf{k} \perp \mathbf{B}$ and $\mathbf{k} \| \langle 111 \rangle$) in a superconducting coil in the orientations $\mathbf{B} \| \langle 110 \rangle$ and $\mathbf{B} \| \langle 211 \rangle$, respectively, at a temperature of 1.5 K. The radiation with frequency ω_{AS} behind the sample was detected as a function of the magnetic field through a grating spectrometer using a HgCdTe detector.

The interband magnetooptical experiments were performed in transmission, using radiation from a liquid nitrogen cooled CO laser (170–240 meV). In the vicinity of the PbSe gap ($E_g = 146$ meV), however, radiation with appropriate frequencies was generated by mixing the radiation of the two CO_2 lasers in an InSb sample ($n = 4 \times 10^{16}\,cm^{-3}$) and using the anti-Stokes radiation the transmission of the PbSe films was measured. These experiments were performed in Faraday ($\mathbf{B} \| \mathbf{k} \| \langle 111 \rangle$) geometry, as well as in Voigt configuration.

In Table 4 the data of the samples are put together.

2.2. *Experimental Results*

Lineshapes of Raman Resonances in the Magnetic Field

Figure 12 shows a registration of the CARS intensity of sample 3 as a function of the magnetic field.

There are four resonances, named a, b, c, d to be seen. The peaks a and b have the lineshape, as drawn in Fig. 7. These resonances are due to strong Raman transitions. The lower levels are occupied by a large number of carriers. From these facts and from the polarization selection rules we conclude that a and b are spin resonances in valleys with large effective

Table 4. Samples

No.	Material	Produced by	Thickness [μm]	Carrier concentration [cm^{-3}]	Mobility [cm^2/Vs]
1	*n*-PbTe	(1)	4.8	1.6×10^{17}	–
2	*n*-PbTe	(1)	54.6	3.0×10^{16}	–
3	*n*-PbTe	(2)	75.2	4.1×10^{16}	32,900[a]
4	*p*-PbTe	(1)	67.3	1.5×10^{17}	290[b]
5	*p*-PbTe	(1)	65.1	2.2×10^{17}	855[b]
6	*n*-PbSe	(3)	20.0	5.5×10^{16}	7,400[a]
7	*n*-PbSe	(3)	19.0	1.6×10^{17}	35,000[a]
8	*n*-PbSe	(3)	5	1.5×10^{17}	–

[a] At 77 K
[b] At 300 K

(1) Prof. Dr. A. Lopez-Otero
(2) Dr. E. Haas
(3) Dr. R. Grisar

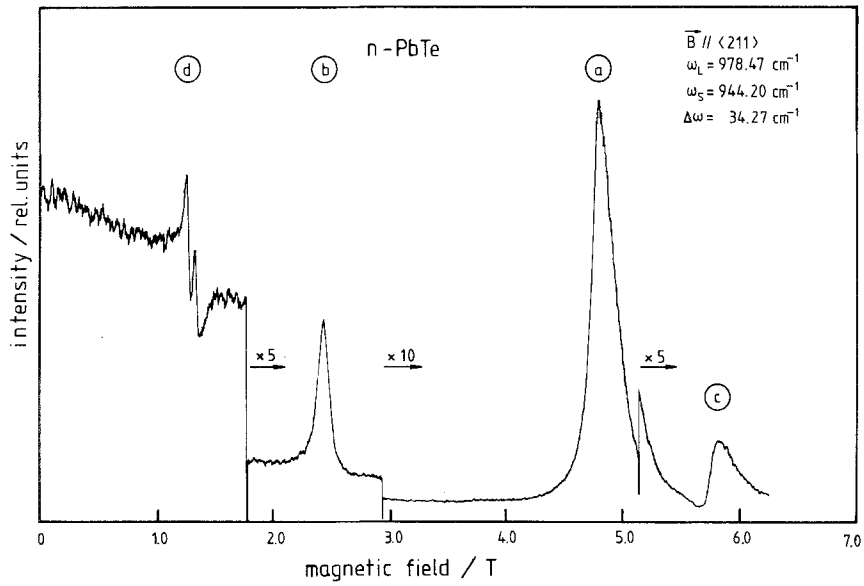

Fig. 12. Coherent anti-Stokes intensity of a PbTe epitaxial film as a function of the magnetic field

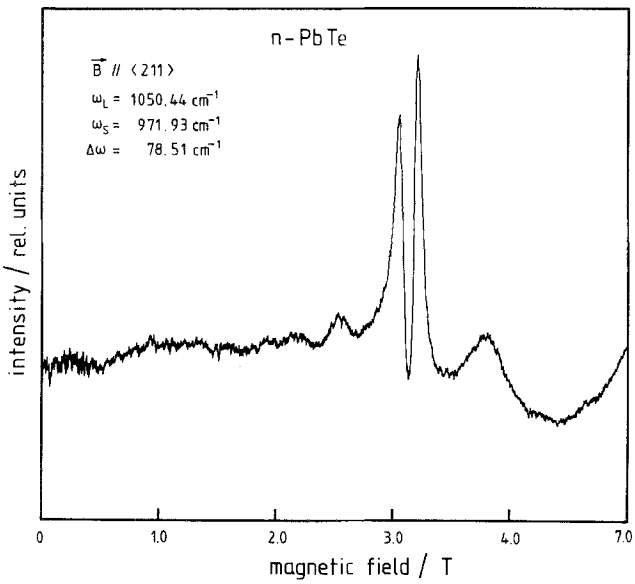

Fig. 13. As Fig. 12 but larger frequency difference $\omega_L - \omega_S$

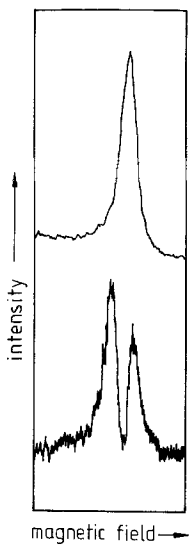

Fig. 14. Dependence of the lineshape of a spin-resonance on the alignment of the beams (*upper trace:* non collinear, phase matching condition partially fullfilled; *lower trace:* exact collinear adjustment of the beams

masses. The resonance d shows the lineshape like Fig. 10. This demonstrates that with this high laser intensity the upper level is higher populated than the lower. The relative minimum in the centre of the resonance, caused by Raman amplification, is very pronounced. Resonance c occurs at about 5.5 T with a lineshape similar to Fig. 8. This is due to a transition the resonant contribution of it is weak, compared to the non-resonant susceptibility.

With larger frequency difference of the two lasers the resonance d occurs at higher magnetic field (Fig. 13). Due to this higher field now the lower level has the higher population. The lineshape is exactly the same, as calculated in Fig. 9. The broad peaks in this figure are due to two-photon resonances of the susceptibility.

In order to find the correct resonance positions for the calculation of the band parameters, one has to compare the experimental registrations with the calculated lineshapes (Figs. 7–10). In the theoretical curves the resonance is assumed to be at 4 T.

i) Dependence of the Lineshape on the Optical Alignment. The upper trace in Fig. 14 shows the resonance b of Fig. 12. Because of the phase factor, (7), even in thin epitaxial films it is convenient to focus the

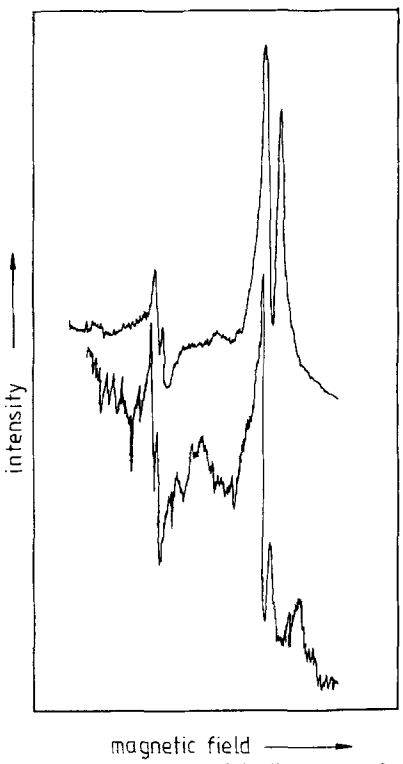

Fig. 15. Dependence of the lineshape of a spin-resonance on the polarization (*upper trace:* $\mathbf{E}_L \perp \mathbf{E}_S$; *lower trace:* $\mathbf{E}_L$ rotated by 10°)

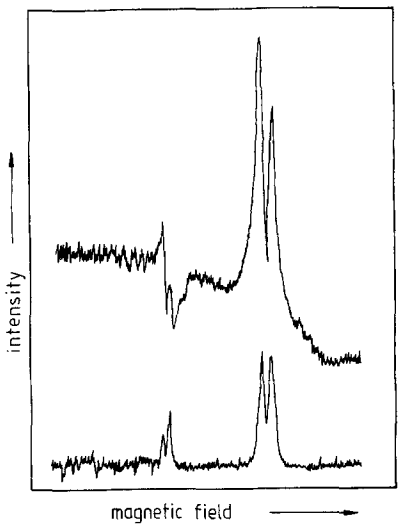

Fig. 16. Dependence of the lineshape of a spin resonance on the laser power (*upper trace:* 2.5 kW; *lower trace:* 0.6 kW)

laser beams with a small angle between them onto the sample. Then the emitted radiation at ω_{AS} is not collinear with the transmitted laser radiation. Therefore the laser radiation is partially cut off by the entrance slit of the spectrometer and strew light is drastically reduced.

In the equations describing Raman amplification no phasefactor is present. Therefore exact collinear adjustment of the laser beams favours Raman amplification above CARS. This is clearly seen in the lower trace of Fig. 14. Now the minimum in the resonance curve occurs and the signal to noise ratio is diminished.

ii) Dependence of the Lineshape on the Polarization of the Laser Radiation. Due to the polarization selection rules the radiation of the lasers has to be polarized orthogonal to one another in order to observe the spin resonance. The intensity of the non-resonant mixing grows by a factor 20 if the lasers are polarized parallel. If the polarization of one laser is rotated by a small angle, e.g. 0.1 rad, the resonant contribution of the susceptibility decreases by $\cos(0.1) = 0.995$ that means 0.5%. The non-resonant part increases by a factor 2. Signals which are dominated by the term $2\chi^{NR}\chi'$, (16), then have twice the amplitude. Resonances, dominated by χ' and χ'', respectively, can get a significant contribution by $2\chi^{NR}\chi'$ and therefore change their lineshape. This is demonstrated by Fig. 15. A rotation of the polarization by 0.2 rad enhances the amplitude of the resonance d (lower magnetic field) by more than a factor 2, whereas the lineshape of resonance c is now similar to d. As can be seen, by this way the sensitivity for weak resonances may be enhanced.

iii) Dependence of the Lineshape on the Laser Intensity. This is demonstrated by the resonance d (lower magnetic field) in Fig. 16. With the high laser power the occupation of the higher level is larger than of the lower one since the lineshape in the upper trace is like Fig. 10. Decreasing the laser power the population is no longer inversed and in the lower trace we observe a lineshape like Fig. 9.

Band Parameters of PbTe

Most of the CARS measurements were carried out with the samples 3 and 5, respectively. The other samples showed exactly the same resonant magnetic fields. From Table 2 it is seen that with $\mathbf{B} \| \langle 110 \rangle$ there are two systems of Landau ladders, with $\mathbf{B} \| \langle 211 \rangle$ three. The resonances are identified by taking into account these facts, the considerations concerning the lineshapes and the transition energies as calculated by the band parameters of other authors [17, 28]. In Fig. 12 the resonance a is due to the transition $0^- \rightarrow 0^+$ (90°), b is the same transition but with $\theta = 61.81°$ and d with $\theta = 19.47°$. Resonance c is caused by the combined spin flip $0^+ \rightarrow 1^-$ (90°).

Table 5. Band parameters of PbTe

Parameter	This work	Ref. [17]
E_g	$(189.7 \pm 0.2) \times 10^{-3}$ eV	0.189 eV
$2P_{\perp}^2/m_0$	6.02 ± 0.05 eV	5.95 eV
a_{cv}	3.42 ± 0.05	3.3 ± 0.2
m_t^+/m_0	-0.102 ± 0.002	-0.095 ± 0.005
m_t^-/m_0	0.060 ± 0.002	0.065 ± 0.005
a^+	3.0 ± 0.3	3.0 ± 0.6
a^-	2.9 ± 0.3	2.7 ± 0.6
g_l^+	-2.61 ± 0.1	1.1 ± 0.2
g_t^+	4.39 ± 0.2	0.35 ± 0.08
g_l^-	1.72 ± 0.2	-2.8 ± 0.6
g_t^-	-1.39 ± 0.2	-1.2 ± 0.3

Table 6. Effective g-factors of PbTe

Angle	Conductionband	Valenceband
19.47°	62.6	62.0
35.26°	54.8	53.0
61.81°	33.6	33.2
90.00°	16.7	13.5
g_l	66.1 ± 0.5	65.6 ± 0.5
g_t	16.7 ± 0.2	13.5 ± 0.2

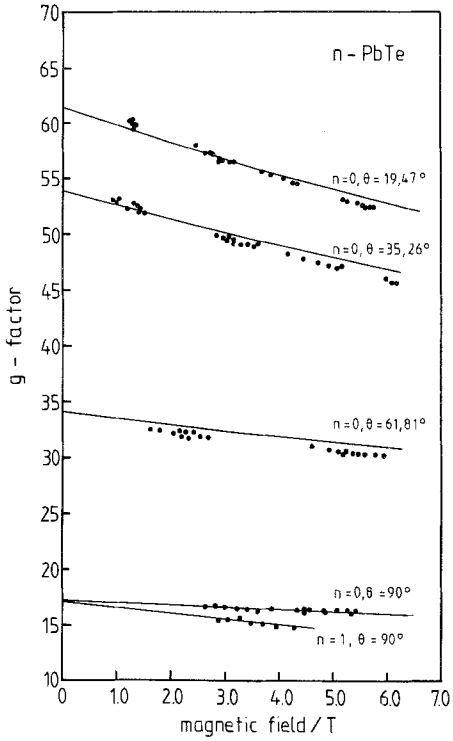

Fig. 17. Effective g-factors of n-PbTe as a function of the magnetic field (— theory; ■ experimental results)

Registrations like Fig. 12 were taken for a large number of frequency differences $\omega_L - \omega_S$. Additionally interband absorption was measured with different CO-laser lines. All these data were fitted and a consistent set of band parameters in the framework of the Mitchell and Wallis model [18] for the conduction and valence band was obtained by a least squares method. The resultant bandparameters are listed in Table 5 in comparison to the values which were previously published. Since the other methods used up to now, like interband-magnetoabsorption and cyclotron resonance, cannot yield precise values of g-factors, it does not surprise that the old values of farband g-factors are wrong. It is seen that even the signs had not been determined correctly. The anisotropy of the farband g-values is very different from the other anisotropies.

Table 6 shows the directly measured effective g-values, extrapolated to the band edge. Due to the narrow linewidths of the spin resonances the experimental error is below 1%. From this table it is seen that the transverse g-factors of the valence- and conduction bands are significantly different and not equal as assumed up to now in the literature. Figures 17 and 18 show the measured effective g-values and full lines, calculated with the band parameters of Table 5.

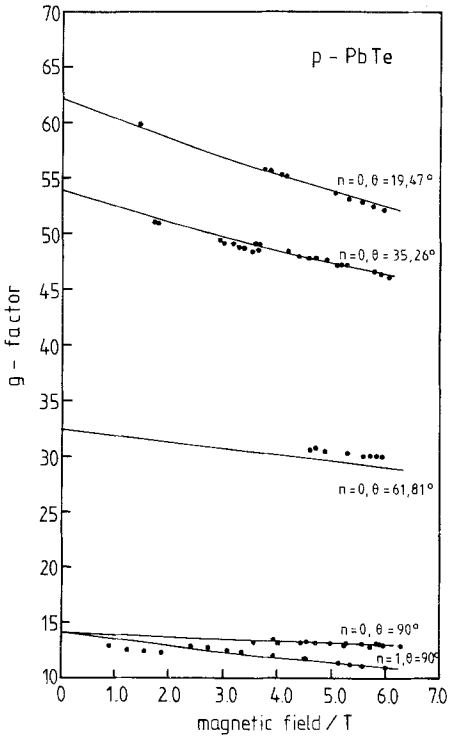

Fig. 18. Effective g-factors (absolute values) of p-PbTe as a function of the magnetic field (— theory; ■ experimental results)

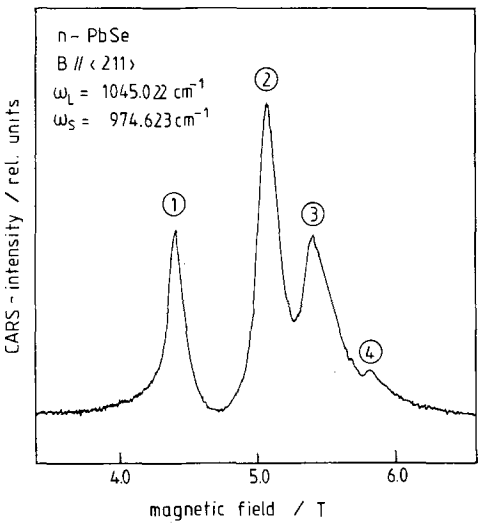

Fig. 19. Registration of the CARS intensity of PbSe; $\mathbf{B} \| \langle 211 \rangle$. ① *cb*, $0^- \rightarrow 0^+$, $\theta = 19.47°$, ② *cb*, $0^- \rightarrow 0^+$, $\theta = 61.81°$, ③ *cb*, $0^- \rightarrow 0^+$, $\theta = 90°$, and ④ *vb*, $0^+ \rightarrow 0^-$, $\theta = 90°$

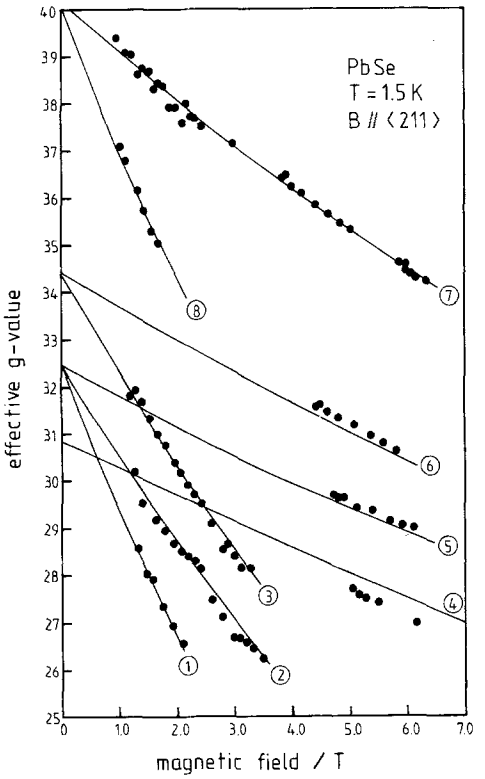

Fig. 20. Effective g-factors (absolute values) of PbSe as a function of the magnetic field. $\mathbf{B} \| \langle 211 \rangle$ (— theory; ■ experimental results.) ① *cb*, $n=2$, $\theta = 90°$; ② *cb*, $n=1$, $\theta = 90°$; ③ *cb*, $n=1$, $\theta = 61.81°$; ④ *vb*, $n=0$, $\theta = 90°$; ⑤ *cb*, $n=0$, $\theta = 90°$; ⑥ *cb*, $n=0$, $\theta = 61.81°$; ⑦ *cb*, $n=0$, $\theta = 19.47°$; ⑧ *cb*, $n=1$, $\theta = 19.47°$

Band Parameters of PbSe

Figure 19 shows a registration of the CARS intensity of the PbSe sample 7. Because the scattered intensity is proportional to the thickness of the sample, squared, it is urged that this sample is only 19 μm thick. The resonance 4 shows that even in n-doped samples valence band transitions can be observed due to photoexcitation of the carriers.

The fitting procedures for PbSe were the same as for PbTe. Table 7 gives the bandparameters and Table 8 the effective masses, the directly measured and extrapolated g-values and the energy gap.

Figures 20 and 21 show the directly measured g-values and full lines calculated from the bandparameters.

Table 7. Band parameters of PbSe

E_g	$2P_\perp^2/m_0$	$P_\perp^2/P_\parallel^2$	
146.3 ± 0.3 meV	3.6 ± 0.1	1.82 ± 0.05	
m_t^+/m_0	m_t^-/m_0	m_l^+/m_t^+	m_l^-/m_t^-
−0.29 ± 0.05	0.27 ± 0.05	1.28 ± 0.2	3.53 ± 0.6
g_t^+	g_l^+	g_t^-	g_l^-
5.4 ± 1	7.3 ± 1	−4.0 ± 1	−8.1 ± 1

Table 8. Band edge values of masses and g-factors of PbSe

E_g	g_t^{vb}	g_t^{cb}	g_l^{cb}
146.3 ± 0.3 meV	30.6 ± 0.3	32.5 ± 0.2	41.08 ± 0.2
m_t^{cb}/m_0	m_l^{cb}/m_0	m_t^{vb}/m_0	m_l^{vb}/m_0
0.0370	0.0685	0.0360	0.0655

Comparison of PbTe and PbSe

The sets of band parameters given in Tables 5 and 7, respectively, yield an excellent agreement between all measured and calculated intra- and interband transitions.

In PbTe the anisotropy $P_\perp^2/P_\parallel^2$ is different from the farband anisotropies g_l^+/g_t^+, g_l^-/g_t^- even by the sign. In PbSe the quotient of the valence band masses differs strongest from $P_\perp^2/P_\parallel^2$. All these differences lead to nonspheriodal shapes of the surfaces of constant energy.

The most striking difference between the band parameters od PbTe and PbSe are the contributions of the farbands to g-values and masses. Whereas in PbTe the values g_l^+, g_t^+, g_l^-, g_t^- are relatively small, in PbSe they reach 25%. On the other hand, in PbTe the farband contributions to the masses are relatively large, in PbSe small.

These differences between the two IV–VI compounds are caused by differences in the level ordering between the two materials. These different level orderings resulted from pseudopotential calculations by Bernick and Kleinman [29]. Their pseudopotential parameters are quite correct for PbSe. With PbTe there are some discrepancies between their values and, e.g. the correct g-factors.

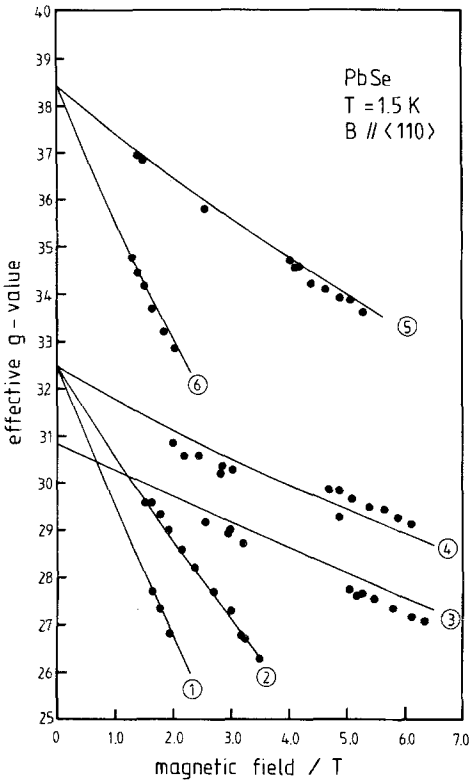

Fig. 21. Effective g-factors (absolute values) of PbSe as a function of the magnetic field. $\mathbf{B} \| \langle 110 \rangle$ (— theory; ■ experimental results). ① *cb*, $n=2$, $\theta=90°$; ② *cb*, $n=1$, $\theta=90°$; ③ *vb*, $n=0$, $\theta=90°$; ④ *cb*, $n=0$, $\theta=90°$; ⑤ *cb*, $n=0$, $\theta=35.26°$; ⑥ *cb*, $n=1$, $\theta=35.26°$

3. Summary

In narrow-gap semiconductors there are very high nonlinear susceptibilities. The third-order susceptibility, responsible for four-wave mixing has a non-resonant part which is inversely proportional to the energy gap and to the square of the effective mass. Non-resonant four-wave mixing in narrow-gap semiconductors therefore is a well suited method to achieve coherent infrared radiation with frequencies where no laser works. Of these facts we took advantage to measure magnetooptical interbandtransitions in PbSe. The third-order nonlinear susceptibility is resonantly enhanced if the frequency difference of the laser beams irradiated onto the sample corresponds to a Raman transition of the scattering medium. Due to interference effects between different nonlinear processes and by changes of the occupation of the states, complicated lineshapes occur. We have calculated those lineshapes in order to find the exact resonance positions within the experimentally observed lines.

We used CARS, one cind of four-wave mixing spectroscopy, to observe magnetooptical intraband transitions. Due to the large values of the susceptibilities in narrow-gap semiconductors even in thin epitaxial layers spin-flip and combined spin-flip resonances could be observed. Because of the small linewidths and since the nonlinear interaction is not affected by phonon and plasmon effects as is the case with spectroscopy in the far infrared, effective g-factors and masses deduced from these measurements are very precise.

We have used these exact results and additionally observed interbandtransitions to fit consistent sets of band parameters of PbTe and PbSe.

Acknowledgements. I express my appreciation to Professor Dr. H. G. Häfele for very useful discussions and encouraging this work. Professor Dr. G. Bauer has communicated to me a lot on the properties of IV–VI compounds. Samples had been given to our disposal by Prof. Dr. A. Lopez-Otero (Universität Linz), Dr. E. Haas (AEG Telefunken, Heilbronn), and Dr. R. Grisar (Frauenhofer Institut für Physikalische Meßtechnik, Freiburg). This work was supported by the "Deutsche Forschungsgemeinschaft". Numerical calculations were performed at the "Rechenzentrum der Universität Würzburg".

List of Most Important Symbols

- $\mathbf{E}$ electric field vector
- $\mathbf{P}$ electric polarization
- ε_0 electric permeability of vacuum: 8.854×10^{-12} F/m
- $\chi^{(n)}$ susceptibility tensor of rank $n+1$
- ε_r dielectric constant
- $\boldsymbol{\sigma}$ conductivity tensor
- μ_0 magnetic permeability of vacuum: 4×10^7 H/m
- i $i^2 = -1$
- ω angular frequency
- $\mathbf{k}$ wave vector
- t time
- I intensity
- g_S Raman gain
- α absorption constant
- E_g energy gap
- e electron electric charge
- m^* effective mass
- E_F Fermi energy
- N carrier density
- Γ linewidth
- $\hbar$ Planck's constant/2π
- $\mathbf{B}$ magnetic displacement vector
- n Landau quantum number
- s spin quantum number

References

1. M. Göppert-Mayer: Ann. Phys. **9**, 273 (1931)
2. P.A. Franken, A.E. Hill, C.W. Peters, G. Weinreich: Phys. Rev. Lett. **7**, 118 (1961)
3. N. Bloembergen: *Nonlinear Optics* (Benjamin, New York 1965)
4. P.N. Butcher, T.P. McLean: Proc. Phys. Soc. **81**, 219 (1963); **83**, 579 (1964)

5. P.N. Butcher, R. Loudon, T.P. McLean: Proc. Phys. Soc. **85**, 565 (1964)
6. D.C. Hanna, M.A. Yuratich, D. Cotter: *Nonlinear Optics of Free Atoms and Molecules*, Springer Ser. Opt. Sci. **17** (Springer, Berlin, Heidelberg 1979)
7. A. Weber (ed.): *Raman Spectroscopy of Gases and Liquids*, Topics Current. Phys. **11** (Springer, Berlin, Heidelberg 1979)
8. C.K.N. Patel, R.E. Slusher, P.A. Fleury: Phys. Rev. Lett. **17**, 1011 (1966)
9. E. Yablonovitch, N. Bloembergen, J.J. Wynne: Phys. Rev. B**3**, 2060 (1971)
10. J.J. Wynne: Phys. Rev. B**6**, 534 (1972)
11. V.T. Nguyen, E.G. Burkhardt, P.A. Wolff: Opt. Commun. **16**, 145 (1976)
    V.T. Nguyen, E.G. Burkhardt: Appl. Phys. Lett. **28**, 187 (1976)
12. M.S. Bresler, O.B. Gusev: Sov. Phys. JETP 49, 363, and 536 (1976)
13. T.J. Bridges, E.G. Burkhardt, V.T. Nguyen: Opt. Commun. **30**, 66 (1979)
14. H. Pascher: Opt. Commun. **41**, 106 (1982)
15. R.L. Aggarwall: In *Physics of High Magnetic Fields*, ed. by S. Chihazumi, N. Miura, Springer Ser. Solid-State Sci. **24** (Springer, Berlin, Heidelberg 1981) p. 105
16. M. Cardona, G. Güntherodt (eds.): *Light Scattering in Solids* II, Topics Appl. Phys. **50** (Springer, Berlin, Heidelberg 1982) and the related Topics Appl. Phys. Vols. 8, 51, and 54
17. G. Bauer: In *Lecture Notes in Physics* **133**, 427 (Springer, Berlin, Heidelberg 1980)
18. D.L. Mitchell, R.F. Wallis: Phys. Rev. **151**, 581 (1966)
19. C.S. DeSilets, C.K.N. Patel: Appl. Phys. Lett. **22**, 543 (1973)
20. S.R.J. Brueck, A. Mooradian: Opt. Commun. **8**, 263 (1973)
21. H. Pascher, G. Appold, R. Ebert, H.G. Häfele: Appl. Phys. **15**, 53 (1978)
22. P.A. Wolff, G.A. Pearson: Phys. Rev. Lett. **17**, 1015 (1966)
23. P. Grosse: *Freie Elektronen in Festkörpern* (Springer, Berlin, Heidelberg, New York 1979)
24. G.L. Eesley: *Coherent Raman Spectroscopy* (Pergamon Press, Oxford 1981)
25. W. Richter: Private communication
26. W. Zawadzki: In *New Developments in Semiconductors*, ed. by P. R. Wallace (Nordhoff, Leyden 1973) p. 441
27. T.Y. Chang: Opt. Commun. **2**, 77 (1970)
28. G. Appold, R. Grisar, G. Bauer, H. Burkhard, R. Ebert, H. Pascher, H.G. Häfele: Inst. Phys. Conf. Ser. **43**, 1101 (1979)
29. R.L. Bernick, L. Kleinman: Solid State Commun. **8**, 569 (1970)